

# Toward a room temperature Schafroth superconductor based on charged excitonic complexes

Z. Sun<sup>1a</sup>, J. Beaumariage<sup>1</sup>, Q. Cao<sup>2</sup>, K. Watanabe<sup>3</sup>, T. Taniguchi<sup>3</sup>, H. Alnatah<sup>1</sup>,  
N. Hougland<sup>1</sup>, J. Chisholm,<sup>1</sup> B. Hunt<sup>2</sup>, I. V. Bondarev<sup>4</sup>, and D. W. Snoke<sup>1</sup>

<sup>1</sup>*Department of Physics and Astronomy, University of Pittsburgh,  
3941 O'Hara St., Pittsburgh, PA 15260, USA*

<sup>2</sup>*Department of Physics, Carnegie Mellon University 15213, USA*

<sup>3</sup>*National Institute for Materials Science, Tsukuba, Ibaraki 305-0044, Japan*

<sup>4</sup>*Department of Mathematics and Physics, North Carolina Central University,  
1801 Fayetteville St., Durham, NC 27707, USA*

In 1954, Schafroth [1] proposed that a Bose condensate of charged bosons should also be a superconductor. Although this ended up not being the explanation of the well known BCS superconductors, the argument is fundamentally sound. In 1996, V.I. Yudson [2] proposed a way to produce a charged boson by attaching two free charges to an exciton in a semiconductor bilayer structure, to make a “quaternion,” or “tetramer.” While that state was never observed in III-V semiconductors, it is predicted to be stable in structures made with monolayers of transition metal dichalcogenide (TMD) materials. Our experimental measurements on structures made from two different TMD materials show a new spectral line at the predicted energy, if and only if all the required conditions for this excitonic complex are fulfilled, including a parallel metal layer that significantly screens the effective interaction between the charge carriers. This suggests a new path for pursuing room temperature superconductivity.

In general, the existence of high-order complexes of charge carriers in semiconductors is well established, including biexcitons (two electrons and two holes) and trions (two electrons and one hole, or vice versa).[3, 4] Biexcitons are charge neutral, however, while trions are fermionic, with half-integer total charge. The lowest-order charged boson therefore consists

---

<sup>a</sup> Current Address: State Key Laboratory of Precision Spectroscopy, East China Normal University, Shanghai 200062, China.

of three negative charges and one positive charge, or vice versa; these will therefore respond to electric field, and a Bose condensate of such complexes should therefore be a superfluid, and therefore also a superconductor. This would be a different mechanism from earlier proposals for exciton-mediated superconductivity — in one proposal [5], it was argued that the presence of a magnetic field would cause neutral excitons to respond to an electric field; in another proposal [6], exciton-polaritons were proposed to play the same role as phonons in Cooper pairs.

The geometry considered by Yudson [2] is shown in Fig. 1 (a). Two semiconductor layers are placed side by side to make a bilayer structure, and this bilayer structure is placed parallel to a nearby metal layer. Under optical pumping, an exciton can be created which then picks up two free electrons (or two holes). At first glance, one would not expect that a complex with three times more negative charge than positive would be stable. The presence of the metal layer, however, produces image charge below the surface, so that much of the repulsive interaction in the quaternion is canceled out.

Like a Bose condensate of excitons, a Bose condensate of quaternions would be metastable to recombination and require optical pumping for steady state. But as the burgeoning field of experimental and theoretical work on Bose condensates of exciton-polaritons has shown [7–11], such a steady-state optical pumped system can indeed undergo condensation, including the effects of superfluidity, and can reach equilibrium in the steady-state with a well-defined temperature [12, 13]. The quaternion particles discussed here do not have a polariton nature, and therefore are more similar to pure exciton condensates, such as interlayer excitons in bilayer systems [14–16], which are subject to much greater disorder effects. However, since the quaternions have charge, they will have much stronger interactions, which may cause a condensate of such particles to be more readily in the Thomas-Fermi regime with a common chemical potential which smooths out the disorder effects.

We consider a variant of the Yudson geometry, which is structurally a trion in one layer bound to a free carrier in a parallel layer, as shown in Fig. 1 (b). Our calculations, discussed below, indicate that this complex is more stable than the Yudson geometry. For the experiments, we fabricated the structure shown in Fig. 1 (c) and (d), based on two-dimensional monolayers of transition-metal dichalcogenides (TMDs). While the original proposal by Yudson was for III-V semiconductor quantum wells, TMD bilayer systems have a number

of advantages. First, the intrinsic exciton binding energy is much larger, of the order of hundreds of meV, and therefore the excitons are stable at room temperature. For example, in the WSe<sub>2</sub> layers used here, the exciton binding energy has been found experimentally to range from 0.1 to 0.8 eV [17–20], depending on the dielectric constant of the surrounding material. Also, hexagonal boron nitride (hBN) can be used as a good insulating barrier to prevent tunneling current while still allowing Coulomb interaction between free carriers in the layers [21].

We have created this structure for several samples, using two different TMD materials, WSe<sub>2</sub> and MoSe<sub>2</sub>, with *p*-doping and *n*-doping, respectively. Figure 1 (d) shows a typical image of the stack of layers for a WSe<sub>2</sub> structure, and Fig. 2 shows the photoluminescence (PL) spectrum for this structure as temperature is varied. We used niobium as the metal,

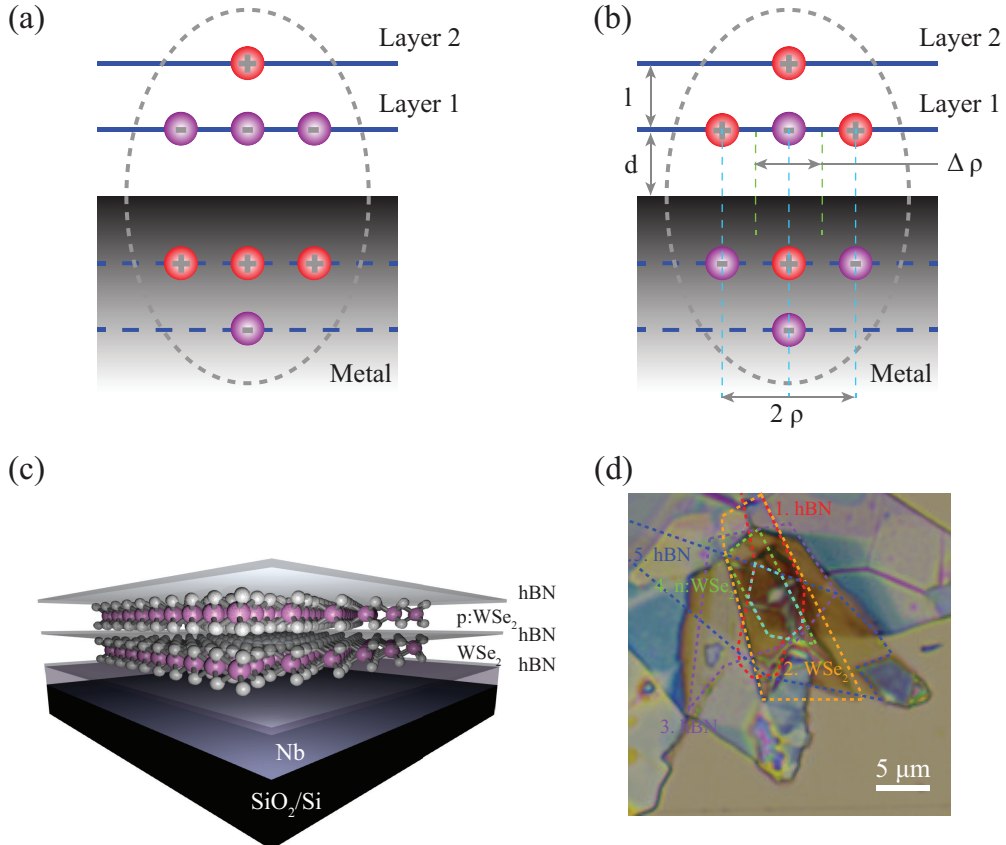


FIG. 1. (a) Quaternion geometry proposed in Ref. 2. The gray region indicates the metallic layer with image charge. (b) Symmetric quaternion geometry considered here. See text for notations. (c) Illustration of the fabricated structure. (d) Image of the structure, with the layers labeled.

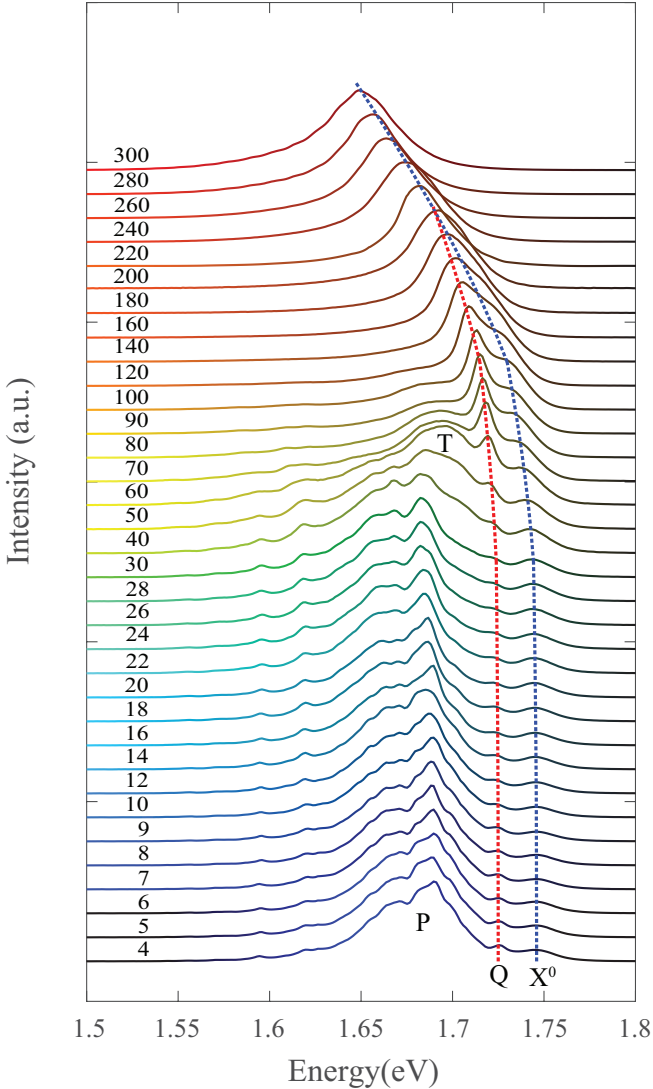


FIG. 2. Normalized photoluminescence spectrum at various temperatures. The dashed lines are fits to the Varshni equation for band gap shift of the lines, discussed in the supplementary information file.  $X^0$  = exciton, T = trion, P = impurity lines, and Q = the candidate for the quaternion emission. The doping density for the p:WSe<sub>2</sub> is  $\sim 10^{17-18}$  cm<sup>-3</sup> (Nb dopant).

with a spacer layer of approximately 15 nm of hBN between the metal and the first TMD monolayer, a layer of approximately 7-nm between the layers, and a capping hBN layer. As seen in Figure 2, a new PL line appears, which we label Q, between the direct exciton line and the trion line, both of which have well-identified energies in these TMD monolayers. As shown below, the energy of the Q line is consistent with calculations of the quaternion binding energy.

We have reproduced this effect in several samples, and have examined a number of control structures; the supplementary information file for this publication gives examples of data from several of these structures. The results can be summarized as follows:

- We have reproduced the new Q line in three different WSe<sub>2</sub> structures with the same design. We have also reproduced it in two structures of the same design but using MoSe<sub>2</sub>, which has the advantage of having much weaker impurity lines.
- The new line appears *only* when the full structure is in place; it never appears when there is no metal layer, or no doping, or only a monolayer.
- We have performed many control experiments with monolayers that confirm the identification of all the other lines we see in WSe<sub>2</sub> and MoSe<sub>2</sub>, namely the single exciton, the trion, the spatially indirect exciton, higher-order complexes such as biexcitons and charged biexcitons, and impurity lines. Figure 3 shows PL spectra for a structure prepared with n:MoSe<sub>2</sub>. An unambiguous peak can be seen in the stack with the metal nearby, while no such peak appears when there is no metal layer.
- We have performed pump-power dependent studies in both WSe<sub>2</sub> and MoSe<sub>2</sub> that show that the new line increases linearly with pump power (see, e.g., Figure S7 of the supplementary file) just as the exciton does, which rules out that it is a biexciton line or an impurity line. Biexciton lines have superlinear behavior with density, as they need two photons to be created; impurity lines have sublinear behavior with increasing pump power.

The change of the intensity of the Q line as temperature changes may be explained by several effects. First, for a quaternion to be formed, an exciton must find two free electrons (or holes), which means that their relative numbers will be determined by a mass-action equation [22]. Second, the number of free carriers will change as a function of temperature; at low temperature, these carriers will mostly be bound to impurities, and therefore the trion and quaternion intensities will drop. Third, at high temperature, all of the PL lines undergo thermal broadening, which makes it hard to distinguish one line from another.

These results, and the identification of the Q line as a quaternion, are consistent with the straightforward theory based on the configuration space method of the binding energy

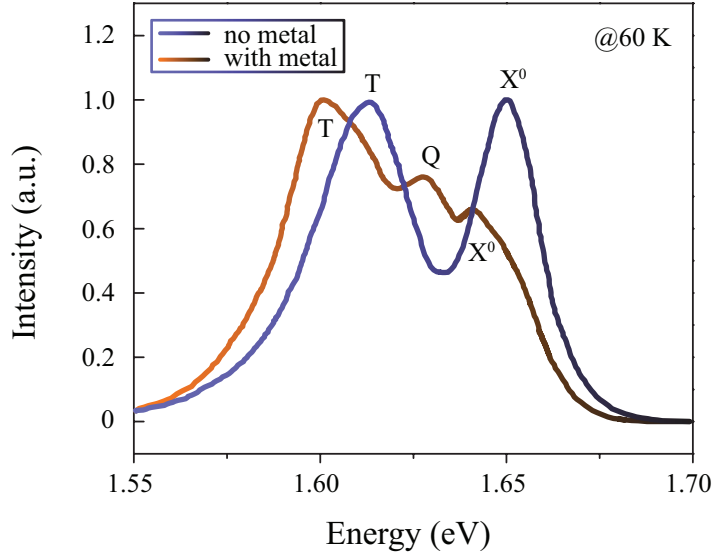


FIG. 3. Normalized photoluminescence spectrum at 60 K for a MoSe<sub>2</sub> stack with and without metal. X<sup>0</sup> = exciton, T = trion, and Q = the candidate for the quaternion emission. The doping density for the n:MoSe<sub>2</sub> is  $\sim 10^{17-18}$  cm<sup>-3</sup> (Re dopant).

calculation [23–25]. The method gives experimentally confirmed binding energies both for interlayer trions [26] and for biexcitons [27] in TMD materials. The configuration-space theory has also been able to explain the evidence for a positive/negative trion binding energy difference [26, 28]. We use it here with the additional inclusion of the image charges in the metal layer. The approach itself was originally pioneered by Landau [29], Gor’kov and Pitaevski [30], Holstein and Herring [31] in their studies of molecular binding and magnetism.

In our model, shown in Fig. 1(b), the intralayer (direct) trion makes the “core” to attach a like charge from the other monolayer to form the quaternion complex. The axial symmetry of such a complex relative to the axis perpendicular to the bilayer, supplemented by the image charges of the same symmetry in metal, makes its ground-state coordinate wave function even (no nodes). In order for a quantum system to remain stable its ground-state wave function must have no nodes [29]. We first calculate the intralayer trion binding energy in the presence of image charges. In the configuration space approach a singly charged exciton complex, i.e., the negative or positive trion, is regarded as a bound system of two equivalent excitons sharing the same hole (or electron) [23]. The trion bound state forms due to the exchange under-barrier tunneling between the equivalent configurations of the

electron-hole system in the configuration space of the two independent relative electron-hole motion coordinates representing the two equivalent excitons separated by the center-of-mass-to-center-of-mass distance  $\Delta\rho$  as sketched in Fig. 1 (b) (see also Fig. S8 of the SI file). The tunnel exchange rate  $J_{X^\pm}$  controls the binding strength. The binding energy of the trion ground state is given by [28]

$$E_{X^\pm}(\sigma, r_0) = -J_{X^\pm}(\Delta\rho = \Delta\rho_{X^\pm}, \sigma, r_0), \quad (1)$$

where the electron-hole mass ratio  $\sigma = m_e/m_h$  and the electrostatic screening length  $r_0$  are the intrinsic parameters of the monolayer, and  $\Delta\rho_{X^\pm}$  is the equilibrium exciton center-of-mass-to-center-of-mass distance in the trion (obtained variationally to maximize the tunnel exchange). We use the Keldysh-Rytova interaction potential for the charges confined in the monolayer to properly account for the screening effect [32]; its screening length  $r_0 = 2\pi\chi_{2D}$  where  $\chi_{2D}$  is the in-plane polarizability of the 2D material [33, 34]. The 3D “atomic units” are used [28–31] with distance and energy expressed in units of the exciton Bohr radius  $a_B^* = 0.529 \text{ \AA} \varepsilon/\mu$  and Rydberg energy  $Ry^* = \hbar^2/(2\mu m_0 a_B^{*2}) = 13.6 \text{ eV } \mu/\varepsilon^2$ , respectively, where  $\varepsilon$  is the effective average dielectric constant of the structure and  $\mu = m_e/(\lambda m_0)$  with  $\lambda = 1 + \sigma$  is the exciton reduced effective mass (in units of the free electron mass  $m_0$ ). The explicit form of  $J_{X^\pm}$  and more theory details can be found in the SI file.

In the presence of a metal, the total potential energy of the intralayer trion is

$$U(\rho, d) = U_0(\rho) + 2 \left( \frac{4}{\sqrt{(2d)^2 + \rho^2}} - \frac{2}{\sqrt{(2d)^2 + (2\rho)^2}} - \frac{3}{2d} \right), \quad (2)$$

where  $\rho$  is the in-plane distance between the hole and the electron shown in Fig. 1 (b), and  $U_0(\rho)$  is the electron-hole potential interaction energy in the absence of a metal already included in Eq. (1). The second term comes from the image charge interaction with  $d$  being the distance of the monolayer from the metal (the distance between the image and the original). For the quaternion, in a similar manner, the total potential energy with the image charge interaction included is

$$\begin{aligned} U(\rho, d, l) = U_0(\rho) + 2 & \left( \frac{4}{\sqrt{(2d)^2 + \rho^2}} - \frac{2}{\sqrt{(2d)^2 + (2\rho)^2}} - \frac{3}{2d} \right. \\ & \left. + \frac{2}{\sqrt{l^2 + \rho^2}} - \frac{1}{l} + \frac{2}{2d + l} - \frac{1}{2d + 2l} - \frac{4}{\sqrt{(2d + l)^2 + \rho^2}} \right), \end{aligned} \quad (3)$$

where  $l$  is the thickness of the spacer layer between the two TMD monolayers — see Fig. 1 (b).

The PL emission spectra in Figures 2 and 3 can be understood in terms of Eqs. (1)–(3). The PL photon energy is given by the initial energy minus the final energy. In the exciton recombination process, the final state is nothing, so the energy of the photon emitted is the bandgap minus the exciton binding energy in the presence of a metal. For the intralayer trion, the final state is a single electron (or hole), which in the presence of a metal has the energy  $2[-1/(2d)]$  due to the image-charge interaction. For the quaternion, there are two final electrons (or two holes), and so the final energy is  $2[-1/(2d)-1/(2d+2l)]$ . Subtracting these final state energies, together with  $U_0(\rho)$ , from  $U(\rho, d)$  and  $U(\rho, d, l)$  in Eqs. (2) and (3), respectively, and adding the intralayer trion binding energy with no metal present of Eq. (1), we obtain the recombination energies of interest in the presence of a metal as functions of  $d$  and  $l$ , which in our experiment are equal to 15 nm and 7 nm, respectively.

Figure 4 (a) shows the recombination energies for the intralayer trion and quaternion as functions of  $d$  and  $l$  calculated in atomic units with the screening parameter  $r_0 = 0.05$  as an example. Apart from the very short  $d$  and  $l$ , the quaternion recombination energy is always above that of the trion as adding an extra like-charge carrier to a charged three-particle system (intralayer trion) results in an extra repulsion in the entire four-particle complex, lowering its binding energy to give an increase in the recombination energy. The quaternion recombination energy goes slowly up as  $d$  increases and down as  $l$  increases, to exceed the exciton recombination energy for  $d$  large enough ( $d=\infty$  is the no-metal case) and to approach the trion recombination energy for  $l$  large enough, which would make it unstable to conversion down to excitons and trions, respectively. Thus, the intervening hBN layer thickness plays a crucial role, and we see all three recombination lines individually because our experimental conditions are different from those of Ref. 19, for example, where a TMD monolayer was placed directly onto a metal.

Figure 4 (b) shows the relative recombination energies for the trion and quaternion in eV, as functions of the distance  $d$  in nanometers. This figure is the cross-section of Fig. 4 (a) converted to physical units with  $l=7$  nm and shifted vertically by choosing the appropriate  $r_0$  to match the 1.89 eV WSe<sub>2</sub> bandgap with the exciton binding energy of 167 meV and the 1.874 eV MoSe<sub>2</sub> bandgap with the exciton binding energy of 231 meV reported recently from precision experiments with TMD monolayers embedded in hBN *without* metal [20],

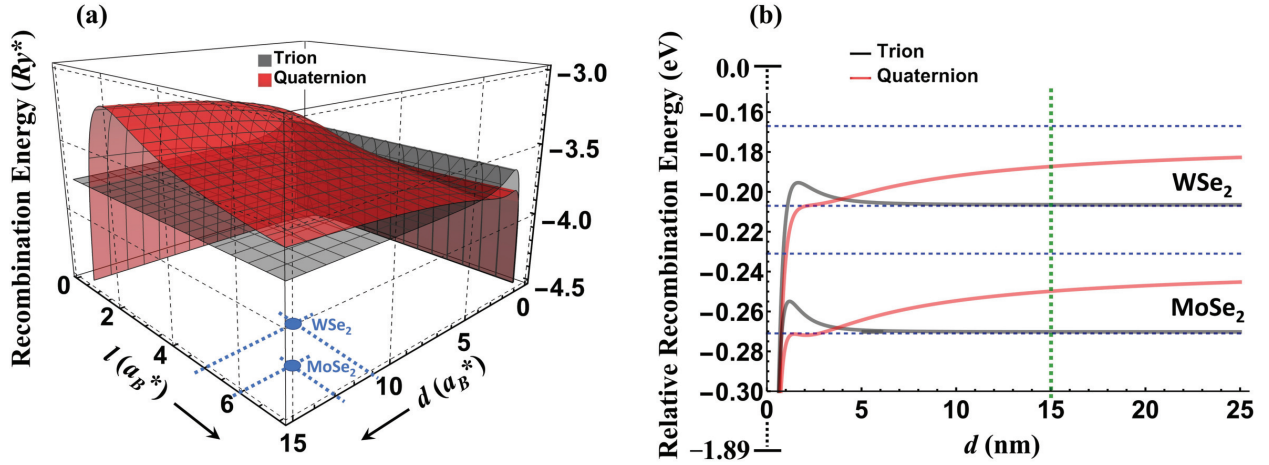


FIG. 4. (a) The recombination energies for the intralayer trion and quaternion as functions of  $d$  and  $l$  in atomic units as given by Eqs. (1)–(3) for  $\sigma=1$  and  $r_0=0.05$ . The blue spots show our experimental  $d$  and  $l$  in these units, determined with  $\varepsilon=5.87$  for WSe<sub>2</sub> and MoSe<sub>2</sub> as described in the text. (b) The trion and quaternion recombination energies for WSe<sub>2</sub> and MoSe<sub>2</sub> relative to their respective bandgaps. The energies are calculated as functions of  $d$  in nanometers for the experimental value of  $l=7$  nm, with  $\varepsilon=5.87$  and  $e\text{-}h$  reduced masses 0.23 (WSe<sub>2</sub>) and 0.27 (MoSe<sub>2</sub>) [36]. The horizontal dotted blue lines trace the exciton binding energies of 167 meV (WSe<sub>2</sub>) and 231 meV (MoSe<sub>2</sub>) [20] and the trion binding energy of 40 meV for both WSe<sub>2</sub> and MoSe<sub>2</sub> we observe. The vertical dashed green line traces  $d=15$  nm in our experiments. See text for details.

which we nicely reproduce, and also to match the 40 meV intralayer trion binding energy we observe both for WSe<sub>2</sub> and for MoSe<sub>2</sub> samples. The figure is obtained for  $\varepsilon=5.87$  assuming that the static dielectric permittivity of our entire system is dominated by the dielectric permittivity of the bulk hBN-material, that is  $\varepsilon=[2\varepsilon_{hBN}(\text{in-plane})+\varepsilon_{hBN}(\text{out-of-plane})]/3$ , where  $\varepsilon_{hBN}(\text{in-plane})=6.93$  and  $\varepsilon_{hBN}(\text{out-of-plane})=3.76$  as was reported recently from advanced numerical simulations [35]. We used the exciton reduced masses  $\mu=0.23$  and 0.27 for WSe<sub>2</sub> and MoSe<sub>2</sub>, respectively, neglecting slight  $e\text{-}h$  effective mass differences [36], to give us  $\sigma=1$  with equal binding energies for the positive and negative trions (see the SI file for more details). With these material parameters we obtain  $a_B^*=1.35$  nm,  $Ry^*=0.09$  eV and  $a_B^*=1.15$  nm,  $Ry^*=0.11$  eV for our WSe<sub>2</sub> and MoSe<sub>2</sub> samples, respectively. Then  $l=7$  nm corresponds to 5.18 in atomic units for the WSe<sub>2</sub> samples and 6.09 in atomic units for the MoSe<sub>2</sub> samples. We use these  $l$  values in Eq. (3), whereby the set of Eqs. (1)–(3) with  $r_0$

fixed provides the crosscuts of Fig. 4 (a) as functions of  $d$  in atomic units. By using  $a_B^*$  and  $Ry^*$  obtained, these functions can be converted to physical units, followed by adjusting  $r_0$  to vertically shift the curves to match the respective WSe<sub>2</sub> and MoSe<sub>2</sub> bandgap energy patterns. We find  $r_0=0.0162$  and  $0.0303$  in atomic units for the WSe<sub>2</sub> and MoSe<sub>2</sub> samples, respectively. We note that our  $r_0$  parameter represents the screening of the like-charge carriers forming the intralayer trion, which are therefore separated by distances at least of the order of  $2a_B^*$ , whereby our  $r_0$  is contributed more by surrounding hBN material than by TMD itself and so it can be quite different from order-of-magnitude greater values reported experimentally for excitons in hBN-embedded TMD monolayers [20]. The low  $r_0$  values we obtain are consistent with the experimental reports of the exciton emission linewidth approaching the homogeneous limit for TMD monolayers embedded in between thick hBN layers [37]. As seen in Fig. 4 (b), both for WSe<sub>2</sub> and for MoSe<sub>2</sub> structures the Q line is located in between the T and X<sup>0</sup> lines. The three lines are well separated in energy, in agreement with what we see in the PL spectra presented in Figs. 2 and 3. We checked that increasing  $\varepsilon$  by a factor as large as 2.5 makes no significant change to the physical picture presented in Fig. 4 (b), showing its robustness thereby. Increasing  $d$  pushes the Q line up to cross over the X<sup>0</sup> line, making the quaternion unstable.

We conclude that the existence of doubly-charged excitonic complexes, or quaternions, in bilayer TMD structures near metallic layers, is to be expected. Our theory shows this complex to be robust to material parameter variation. Our spectroscopic studies give a candidate spectral line in full agreement with the theory predictions; all of the other lines which we observe spectroscopically can be identified as known lines, as discussed in the Supplementary Information. Further confirmation of the identification of the quaternion states may be obtained by observing their motion in response to an in-plane electric field, since they have net charge, or by two-dimensional spectroscopy methods.

The question remains what would be needed to have a realistic room temperature superconductor made from a condensate of quaternions. BEC occurs generally at high density, which means that experiments with high excitation intensity could push the quaternion density high enough for condensation, but at high density, nonradiative collisional Auger recombination may become important. It may be that mixing these quaternion states resonantly with photons to create a polaritonic state could be the best path toward condensation;

the polariton effect also reduces the effective mass of the particles, which reduces the needed density for condensation and also averages over disorder on length scales of the wavelength of light [16]. Although true BEC is not possible in one and two dimensions for noninteracting bosons [38], it is known that a slight lateral confinement enables BEC for noninteracting bosons both in 2D and in 1D [39, 40], and in general, in any finite system in which the size of the system is small compared to the coherence length, the system can undergo a transition indistinguishable from BEC. Another interesting question is how the long-range Coulomb interaction of doubly-charged quaternions affects their condensation. Our results here indicate that quaternion physics in bilayer systems with metal layers is a promising field of research.

**Methods** Isolated monolayer WSe<sub>2</sub> and MoSe<sub>2</sub> with a typical size of  $5 \times 15 \mu\text{m}^2$  were mechanically exfoliated from bulk crystals (purchased from 2D Semiconductors). The whole samples were fabricated by the standard dry transferring method to the surface of substrates. The thin film of Ni was grown by the e-beam evaporator with a typical thickness of 150 nm on top of the 90 nm SiO<sub>2</sub> coating Silicon (purchased from the Graphene Supermarket). The thicknesses of the hBN were characterized by AFM (Bruker Dimesnison Icon).

**Acknowledgements.** This work was supported by the US Army Research Office under MURI award W911NF-17-1-0312 (Z.S., J.B, D.W.S.) and by the U.S. Department of Energy, Office of Science, Office of Basic Energy Sciences, under award number DE-SC0007117 (I.V.B). K.W. and T.T. acknowledge support from the EMEXT Element Strategy Initiative to Form Core Research Center, Grant Number JPMXP0112101001 and the CREST(JPMJCR15F3), JST. B.M.H. and Q.C. were supported by the Department of Energy under the Early Career Award program (#DE-SC0018115).

**Author contributions** Z.S. and D.S. initiated the project. Z.S., D.S. and J.B. designed the experiments. Z.S., C.R., H.A., N.H. and J.C. fabricated the quaternion samples and the control samples, Z.S. J.B., H.A., N.H. and J.C. collected the optical characterization data, and Z.S., D.S. and I.B. analysed the data. I.B. carried out the theoretical modelling. All the authors contributed to the discussion of the results and writing the manuscript.

**Corresponding author** Correspondence to Zheng Sun.

---

[1] M.R. Schafroth, Physical Review **96**, 1442 (1954).

[2] V.I. Yudson, Phys. Rev. Lett. **77**, 1564 (1996).

[3] F. Pulizzi, D. Sanvitto, P.C.M. Christianen, A.J. Shields, S.N. Holmes, M.Y. Simmons, D.A. Ritchie, M. Pepper, and J.C. Maan, Phys. Rev. B **68**, 205304 (2003).

[4] Z. Li, T. Wang, Z. Lu, C. Jin, Y. Chen, Y. Meng, Z. Lian, T. Taniguchi, K. Watanabe, S. Zhang, D. Smirnov and S.-F. Shi, Nature Comm. **9**, 3719 (2018).

[5] Yu.E. Lozovik and V. Yudson, Sov. Phys. JETP. **44**, 389 (1976).

[6] O. Cotlet, S. Zeytinoglu, M. Sigrist, E. Demler, and A. Imamoglu, Phys. Rev. B **93**, 054510 (2016).

[7] J. Kasprzak, M. Richard, S. Kundermann, A. Baas, P. Jeanbrun, J.M.J. Keeling, R. André, J.L. Staehli, J.L., V. Savona, P.B. Littlewood, B. Deveaud, and L.S. Dang, Nature **443**, 409 (2006).

[8] R. Balili, V. Hartwell, D.W. Snoke, L. Pfeiffer and K. West, Science **316**, 1007 (2007).

[9] H. Deng, H. Haug, and Y. Yamamoto, Rev. Mod. Phys. **82**, 1489 (2010).

[10] I. Carusotto and C. Ciuti, Rev. Mod. Phys. **85**, 299 (2013).

[11] D. Snoke and J. Keeling, Physics Today **70**, 54 (2017).

[12] Y. Sun, P. Wen, Y. Yoon, G.-Q. Liu, M. Steger, L.N. Pfeiffer, K. West, D.W. Snoke, and K.A. Nelson, Phys. Rev. Lett. **118**, 016602 (2017).

[13] D. Caputo, D. Ballarini, G. Dagvadorj, C. Sánchez Muñoz, M. De Giorgi, L. Dominici, K. West, L.N. Pfeiffer, G. Gigli, F.P. Laussy, M.H. Szymanska, and D. Sanvitto, Nature Materials **17**, 145 (2018).

[14] M. Combescot, R. Combescot, and F. Dubin, Rep. Prog. Phys. **80**, 066501 (2017).

[15] Yu.E. Lozovik, Physics Uspekhi **61**, 1094 (2018).

[16] D.W. Snoke, in *Quantum Gases: Finite Temperature and Non-Equilibrium Dynamics*, N.P. Proukakis, S.A. Gardiner, M.J. Davis, and M.H. Szymanska, eds. (Imperial College Press, London, 2013).

[17] K. He, N.Kumar, L. Zhao, Z. Wang, K.F. Mak, H. Zhao, and J. Shan Phys. Rev. Lett. **113**, 026803 (2014).

- [18] A.T. Hanbicki, M. Currie, G. Kioseoglou, A.L. Friedman, and B.T. Jonker, Solid State Comm. **203**, 16 (2015).
- [19] S. Park, N. Mutz, T. Schultz, S. Blumstengel, A. Han, A. Aljarb, L.-J. Li, E.J.W. List-Kratochvil, P. Amsalem, and N. Koch, 2D Mater. **5**, 025003 (2018).
- [20] M.Goryca, J.Li, A.V.Stier, T.Taniguchi, K.Watanabe, E.Courtade, S.Shree, C.Robert, B.Urbaszek, X.Marie, and S.A.Crooker, Nature Commun. **10**, 4172 (2019).
- [21] A. Raja, A. Chaves, J. Yu, G. Arefe, H.M. Hill, A.F. Rigos, T.C. Berkelbach, P. Nagler, C. Schller, T. Korn, C. Nuckolls, J. Hone, L.E. Brus, T.F. Heinz, D.R. Reichman, and A. Chernikov, Nature Comm. **8**, 8, 15251 (2017).
- [22] D.W. Srolovitz, *Solid State Comm.* **146**, 73 (2008).
- [23] I.V. Bondarev, Mod. Phys. Lett. B **30**, 1630006 (2016).
- [24] I.V. Bondarev, Phys. Rev. B **83**, 153409 (2011); Phys. Rev. B **90**, 245430 (2014).
- [25] I.V. Bondarev and M.R. Vladimirova, Phys. Rev. B **97**, 165419 (2018).
- [26] L.A. Jauregui, A.Y. Joe, K. Pistunova, D.S. Wild, A.A. High, Y. Zhou, G. Scuri, K. De Greve, A. Sushko, C.-H. Yu, T. Taniguchi, K. Watanabe, D.J. Needleman, M.D. Lukin, H. Park, and P. Kim, Science **366**, 870 (2019).
- [27] M. Kremser, M. Brotons-Gisbert, J. Knörzer, J. Glückelhorn1, M. Meyer, M. Barbone, A.V. Stier, B.D. Gerardot, K. Müller, and J.J. Finley, npj 2D Materials and Applications **4**, 8 (2020).
- [28] I.V. Bondarev, O.L. Berman, R.Ya. Kezerashvili, and Y.E. Lozovik, arXiv:2002.09988.
- [29] L.D.Landau and E.M. Lifshitz, *Quantum Mechanics. Non-Relativistic Theory* (Pergamon, Oxford, 1991).
- [30] L.P.Gor'kov and L.P. Pitaevski, Dokl. Akad. Nauk SSSR **151**, 822 (1963) [English transl.: *Soviet Phys.—Dokl.* **8**, 788 (1964)].
- [31] C.Herring, Rev. Mod. Phys. **34**, 631 (1962); C.Herring and M.Flicker, Phys. Rev. **134**, A362 (1964).
- [32] L.V. Keldysh, Sov. Phys. JETP **29**, 658 (1979); N.S. Rytova, Proc. MSU Phys. Astron. **3**, 30 (1967).
- [33] T.C. Berkelbach, M.S. Hybertsen, and D.R. Reichman, Phys. Rev. B **88**, 045318 (2013).
- [34] P. Cudazzo, I.V. Tokatly, and A. Rubio, Phys. Rev. B **84**, 085406 (2011).

- [35] A. Laturia, M.L. Van de Put, and W.G. Vandenberghe, *2D Materials and Applications* **2**, 6 (2018).
- [36] F.A. Rasmussen and K.S. Thygesen, *J. Phys. Chem. C* **119**, 13169 (2015).
- [37] F. Cadiz, E. Courtade, C. Robert, G. Wang, Y. Shen, H. Cai, T. Taniguchi, K. Watanabe, H. Carrere, D. Lagarde, M. Manca, T. Amand, P. Renucci, S. Tongay, X. Marie, and B. Urbaszek, *Phys. Rev. X* **7**, 021026 (2017).
- [38] P.C. Hohenberg, *Phys. Rev.* **158**, 383 (1967).
- [39] V. Bagnato and D. Kleppner, *Phys. Rev. A* **44**, 7439 (1991); W.-S. Dai and M. Xie, *Phys. Rev. A* **67**, 027601 (2003).
- [40] I.V. Bondarev and A.V. Meliksetyan, *Phys. Rev. B* **89**, 045414 (2014).

# Supplementary Information for “Toward a room temperature Schafroth superconductor based on charged excitonic complexes”

Z. Sun<sup>1a</sup>, J. Beaumariage<sup>1</sup>, Q. Cao<sup>2</sup>, K. Watanabe<sup>3</sup>, T. Taniguchi<sup>3</sup>, H. Alnatah<sup>1</sup>,  
N. Hougland<sup>1</sup>, J. Chisholm,<sup>1</sup> B. Hunt<sup>2</sup>, I. V. Bondarev<sup>4</sup>, and D. W. Snoke<sup>1</sup>

<sup>1</sup>*Department of Physics and Astronomy, University of Pittsburgh,  
3941 O’Hara St., Pittsburgh, PA 15260, USA*

<sup>2</sup>*Department of Physics, Carnegie Mellon University 15213, USA*

<sup>3</sup>*National Institute for Materials Science, Tsukuba, Ibaraki 305-0044, Japan*

<sup>4</sup>*Department of Mathematics and Physics, North Carolina Central University,  
1801 Fayetteville St., Durham, NC 27707, USA*

## I. EXPERIMENTAL PHOTOLUMINESCENCE SPECTRA

Figures S1 to S5 show the PL spectra of various samples as temperature is varied. The curves are labeled by the bath temperature in each case. In all figures, X<sup>0</sup> indicates the direct exciton line, P indicates impurity lines, T indicates the trion line, Q indicates the proposed quaternion line, and IX indicates the spatially indirect exciton line. In Figure S4, B indicates the intralayer biexciton line, based on the identification of Ref. 1.

### A. Varshni formula for the band gap shift with temperature

The shift of the lines with temperature in Fig. 2 of the main text and Fig. S1 are fit with the well-established Varshni formula for band gap shift, based on the many-body renormalization of the states due to phonon interaction (see Section 8.3 of Ref. 2):

$$E(T) = E(0) - \frac{\alpha T^2}{T + \beta},$$

where  $\alpha$  is a parameter giving the interaction strength of the state under consideration with optical phonons, and  $\beta$  is a parameter approximately equal to the average optical phonon

---

<sup>a</sup> Current Address: State Key Laboratory of Precision Spectroscopy, East China Normal University, Shanghai 200062, China.

	doped bilayer with metal (Sample 1)	(Sample 2)	undoped monolayer	doped monolayer	doped monolayer with metal	doped bilayer without metal	Ref. 1
$X^0$	1.746	1.747	1.725	1.720	1.745	1.745	1.745
Q	1.725	1.730	—	—	—	—	—
T	1.70	1.70	—	1.68	1.69	1.70	1.71
P	1.6-1.7	1.6-1.7	1.6-1.7	1.55-1.7	1.55-17	1.6-1.7	1.6-1.7
$B^-$	—	—	—	—	1.651*	1.66**	1.68

TABLE I. Measured values of the various excitonic complex spectral lines for WSe<sub>2</sub>, in electron-Volts (eV), at  $T = 4$  K.  $X_0$  = direct intralayer exciton; T = intralayer trion; Q = quaternion candidate; P = impurity lines (the total spectral range is given);  $B^-$  = charged biexciton (\*data at  $T = 100$  K; \*\*data at  $T = 60$  K). Data from Ref. 1 are for  $T = 10$  K.

energy in units of Kelvin. For the fits shown, we used  $\beta = 328$  K, which is consistent with the measured optical phonon energy in WSe<sub>2</sub> of 31 meV [3], and  $\alpha = 0.00069$  for the exciton state and  $\alpha = 0.00043$  for the quaternion state. For the data of Figure 2 of the main text,  $E(0) = 1.746$  eV for the exciton and  $E(0) = 1.725$  eV for the quaternion, while for the data of Figure S1 here,  $E(0) = 1.7463$  eV for the exciton and  $E(0) = 1.73$  eV for the quaternion, reflecting the effect of slightly different dielectric constant for the environment of the layers.

## B. Summary of observed excitonic transitions

Table I summarizes the peak energies of the spectral lines we observe in WSe<sub>2</sub> at low temperature. The candidate quaternion line we see cannot be identified as any of the following:

- Impurity lines are seen even without the metal layer (see Figs. S2, S3, and S5) at energies in agreement with previous work on 2D monolayers [4], and occur only at low temperature.
- The intralayer trion line showing up at 1.7 eV at elevated temperatures is well identified in other works [5] and occurs separately from the new line, and coexists with it (e.g., at  $T \sim 80 - 100$  K in Fig. 2 of the main text).

- Intralayer biexcitons, formed from two excitons both in the same layer, were initially thought to occur at much lower energy, in the same range as the impurity lines [1], but recent work [24–27] has observed evidence for an intralayer biexciton line much nearer to the direct exciton line, in the same spectral range as our quaternion line. However, in those experiments, the biexciton line was seen in monolayers, and had the telltale dependence of intensity going as the square of the exciton intensity, which is expected since two excitons must collide to form a biexciton. In our experiments, the quaternion line is never seen in a monolayer, and has a linear dependence of its intensity, as shown in Fig. S7. The reason for the difference in the experiments is that the experiments showing the biexciton line took great care to have undoped layers with negligible free carrier density, while ours used a *p*-doped layer. It is actually quite difficult to observe intralayer biexcitons in WSe<sub>2</sub>, and most experiments do not observe this line. In the presence of free carriers, the intralayer biexciton is unstable toward formation of charged biexcitons, discussed below.
- Surprisingly, there is evidence [25] of stable *five*-carrier complexes, made of two excitons plus one extra charge. This shows that the idea of a family of excitonic complexes with 2, 3, 4, and even 5 carriers in a bound state is now standard for TMD materials. The charged biexciton in WSe<sub>2</sub> shows up in monolayers, and is at much lower energy than the intralayer exciton, around 1.65 eV. We see evidence for this line in Figures S4 and S5.
- Interlayer exciton lines occur at much lower energy due to the band offset between the layers, because the PL photon emitted comes from an interlayer recombination process, as confirmed by other works [6] and by our own work with related samples (see Fig. S5 and Ref. 7). In bilayer structures with and without a metal layer, the appearance of an indirect (interlayer) exciton line is a strong function of the thickness of the hBN layer between the TMD layers; for a 2-nm layer the indirect exciton line appears prominently (Fig. S5), while for a 7-nm layer, as used in the structure of Fig. 1(d) of the main text, there is no discernible indirect exciton line. The identification of the indirect exciton line in this and other samples was confirmed by lifetime measurements showing it has much longer lifetime than the direct exciton [7].

- Charged interlayer excitons, which we do not see, consisting of two holes in one monolayer and one electron in the other monolayer (or vice versa), require a thinner interlayer spacer to be visible spectroscopically ( $\sim 1$  nm as opposed to 7 nm we have in the sample used for Fig. 2 of the main text). They will also have the PL energy shifted down, below the interlayer exciton line, since their PL process requires an interlayer exciton to recombine. They also have small binding energies ( $\sim 10 - 15$  meV demonstrated both theoretically and experimentally [6, 9]).
- Interlayer biexcitons require high excitation power and so far were only observed in laterally confined TMD bilayers [8] due to their vanishingly small binding energy [9]. They would not be stabilized by the presence of a metal either because of their overall electrical neutrality.
- The trion state formed by the exciton in one monolayer and a hole (or electron) in the other monolayer cannot show up in our spectra as such a state possesses no intrinsic axial symmetry necessary for it to be stable. From general quantum mechanics, the ground state of a stable quantum system must have no nodes [10]. For a few-particle complex to be stable, its coordinate wave function has to be even (no nodes), which in our case can only occur if the complex has an axially symmetric charge distribution relative to the axis perpendicular to the bilayer. This main feature of the quaternion complex we claim to observe is totally absent from such a trion complex. Adding a metal does not change the symmetry and so does not help stabilize this trion state.

## II. THEORY FOR TRION BINDING ENERGY CALCULATIONS WITH NO METAL PRESENT

### A. General Case: Charged InterLayer Exciton in Bilayers

We start with the most general case of the Charged Interlayer Exciton (CIE) binding energy calculation presented lately by one of us (with coauthors) in Ref. [12]. Only a brief outline of the theory is provided here; see Refs. [9, 11, 12] for particulars. A sketch of the CIE — (interlayer) trion — in a TMD bilayer is shown in Fig. S8 (a) for the negative trion

case; the positive trion can be obtained by charge sign inversion. In Figure S8 and *all over throughout this section*, the interlayer separation distance  $d$  is not to be confused with the monolayer-to-metal distance shown in Fig. 1 (b) of the main text.

The CIE is a charged three-particle complex of an interlayer (indirect) exciton (IE) and an extra hole ( $h$ ) or electron ( $e$ ), in which two like-charge carriers confined to the same layer share an unlike-charge carrier from the other layer. Such a CIE complex can be viewed as being formed by the *two* equivalent indistinguishable symmetric IE configurations with an extra charge carrier attached to the left or right IE. For such a quantum system, the effective configuration space can be represented by the two *independent* in-plane projections  $\rho_1$  and  $\rho_2$  of the relative  $e$ - $h$  coordinates in each of the IEs as can be seen from the comparison of Fig. S8 (a) and (b). The CIE bound state then forms due to the exchange under-barrier tunneling in the configuration space  $(\rho_1, \rho_2)$  between the two *equivalent* IE configurations of the  $e$ - $h$  system that are separated by the IE center-of-mass-to-center-of-mass (CM) distance  $\Delta\rho$ . The binding strength is controlled by the exchange tunneling rate integral of the form [12]

$$J_{X^\pm}(\Delta\rho, \sigma, r_0, d) = 2N^4\Delta\rho^2 \exp\left[-2\alpha\left(\sqrt{\Delta\rho^2 + 4d^2} - 2d\right)\right] \quad (1)$$

$$\times \left[ \frac{\alpha}{\sqrt{\Delta\rho^2 + 4d^2}} + \frac{1}{2\left(r_0 + \left\{ \frac{1}{\sigma} \right\} \Delta\rho/\lambda\right)(\alpha\Delta\rho - 1)} \right] \left( \frac{r_0 + \left\{ \frac{1}{\sigma} \right\} \Delta\rho/\lambda}{r_0 + \Delta\rho} \right) \overline{\left\{ \frac{\sigma}{1} \right\} (\alpha\Delta\rho - 1)}$$

with

$$\alpha = \frac{2}{1 + 2\sqrt{d}} \quad \text{and} \quad N = \frac{4}{\sqrt{1 + 4\sqrt{d} + 8d(1 + \sqrt{d})}} \quad (2)$$

being the interlayer-separation dependent constants coming from the IE wave function [13], and the upper or lower term is to be taken in the curly brackets for the positive or negative CIE, respectively. Here the 3D "atomic units" are used [9, 11, 12], with distance and energy measured in the units of the exciton Bohr radius  $a_B^* = 0.529 \text{ \AA} \varepsilon/\mu$  and the exciton Rydberg energy  $Ry^* = \hbar^2/(2\mu m_0 a_B^{*2}) = e^2/(2\varepsilon a_B^*) = 13.6 \text{ eV} \mu/\varepsilon^2$ , respectively,  $\varepsilon$  represents the *effective* average dielectric constant of the bilayer heterostructure and  $\mu = m_e/(\lambda m_0)$  stands for the exciton reduced effective mass (in units of free electron mass  $m_0$ ) with  $\lambda = 1 + m_e/m_h = 1 + \sigma$ .

To properly take into account the screening effect for the electrostatic interaction of like

charges in monolayers [14–16], in deriving Eq. (1) the Keldysh-Rytova (KR) electrostatic potential interaction energy is used in the form

$$V_{\text{KR}}(\rho) = \frac{\pi}{(\epsilon_1 + \epsilon_2)r_0} \left[ H_0\left(\frac{\rho}{r_0}\right) - N_0\left(\frac{\rho}{r_0}\right) \right], \quad (3)$$

which we approximate in terms of elementary functions as follows (atomic units)

$$V_{\text{eff}}(\rho) = \frac{1}{r_0} \left[ \ln\left(1 + \frac{r_0}{\rho}\right) + (\ln 2 - \gamma)e^{-\rho/r_0} \right]$$

as was previously proposed for atomically thin layers in Ref. [17]. Here,  $\rho$  is the in-plane intercharge distance,  $r_0 = 2\pi\chi_{2D}$  is the screening length parameter with  $\chi_{2D}$  being the in-plane polarizability of 2D material, and  $\epsilon_{1,2}$  are the dielectric permittivities of its surroundings. For unlike charges, their screened interlayer electrostatic potential interaction energy is taken to be (atomic units)

$$V_{\text{C}}(r) = -\frac{1}{r} = -\frac{1}{\sqrt{\rho^2 + d^2}} \quad (4)$$

as dictated by the classical electrostatic Coulomb interaction of two space-separated point charges with intercharge distance written in cylindrical coordinates.

The function  $J_{X^\pm}$  in Eq. (1) is clearly seen to have a maximum as  $\Delta\rho$  and  $d$  vary. It tends to become a negative when  $\alpha\Delta\rho < 1$  in the second term in the square brackets, which is always the case for  $d$  large enough whereby  $\alpha \approx 1/\sqrt{d} \sim 0$  per Eq. (2), making the second term in the square brackets negative and the first term negligible; whereas for  $\alpha\Delta\rho > 1$  it is manifestly positive and approaching zero as  $\Delta\rho$  increases. As an example, in Fig. S9 (a) we show the actual behavior of the tunneling exchange integral  $J_{X^\pm}$  as a function of  $d$  and  $\Delta\rho$ , calculated per Eqs. (1) and (2) with  $d$  chosen to be in the range not to exceed typical van der Waals interlayer separations (3 ÷ 6 Å in atomic units). In the case of the CIE,  $\Delta\rho > 1$  is the physically meaningful  $\Delta\rho$  domain [9, 12]. Seeking the extremum for  $J_{X^\pm}(\Delta\rho)$  under this condition (with all other parameters fixed) can be done with *only* the leading terms in small  $1/\Delta\rho$  included in the procedure. This gives the equilibrium value of  $\Delta\rho$  as follows [12]

$$\Delta\rho_{X^\pm} = \frac{7\alpha - 1 - \left\{ \frac{\sigma}{1/\sigma} \right\}}{2\alpha^2} - \left( 3 + 2 \left\{ \frac{\sigma}{1/\sigma} \right\} \right) r_0. \quad (5)$$

Substituting Eq. (5) in Eq. (1) and reversing the sign of the result, gives the positive and negative CIE binding energies as indicated by Eq. (1) in the main text. The equilibrium ratio  $d/\Delta\rho_{X^\pm}$  calculated from Eq. (5) is shown in Fig. S9 (b).

The electrostatic interaction potential energies (3) and (4) can be shown to consistently originate from the general solution to the electrostatic boundary-value problem that includes two coupled parallel monolayers. Such a solution was recently found and presented in Ref. [19] (Appendix A). A bilayer system was considered to consist of the two parallel monolayers with individual 2D-polarizabilities  $\chi'_{2D}$  and  $\chi''_{2D}$  (in our notations) that are separated by a distance  $d$  and surrounded by a dielectric medium of the static permittivity  $\varepsilon$ , with a point charge sitting at the origin of the cylindrical coordinate system placed in the bottom layer. In order to find the electrostatic interaction potential energy in the whole space, the Poisson's equation was solved in the Fourier space in the way similar to that reported in Ref. [17]. In the 2D-coordinate space, the solution obtained yields the electrostatic unlike- and like-charge interaction energies of interest as follows (atomic units)

$$V_{2D}(\rho, d) = - \int_0^\infty \frac{dq J_0(q\rho) e^{-qd}}{(1 + qr'_0)(1 + qr''_0) - q^2 r'_0 r''_0 e^{-2qd}}, \quad (6)$$

$$V_{2D}(\rho, 0) = \int_0^\infty \frac{dq J_0(q\rho) [1 + qr''_0(1 - e^{-2qd})]}{(1 + qr'_0)(1 + qr''_0) - q^2 r'_0 r''_0 e^{-2qd}},$$

where  $r'_0 = 2\pi\chi'_{2D}$  and  $r''_0 = 2\pi\chi''_{2D}$  are the respective screening parameters for the individual monolayers. Due to the presence of the second layer, these equations do not seem to look similar to the solitary-monolayer KR interaction case in Eq. (3) we use. However, setting  $d=\infty$  to take the top layer away makes the former zero, while the latter integrates to yield the KR potential energy (3) with the effective screening length  $r_0 = r'_0$  just as it should be.

Due to the oscillatory behavior of the 0th order Bessel function  $J_0(x)$  for all  $x > 1$ , only  $q \lesssim 1/\rho$  contribute the most to the integrals in Eq. (6). In our case,  $\rho \approx \Delta\rho_{X^\pm}$  as can be seen from Fig. S8 (a). Then, in the domain  $1/\Delta\rho_{X^\pm} < 1$  which Eqs. (1) and (5) are obtained for [9, 12], one has  $q \lesssim 1/\rho \approx 1/\Delta\rho_{X^\pm} < 1$  to contribute the most to both integrals, so that  $qd \lesssim d/\Delta\rho_{X^\pm} < 1$  which is indeed the case as Fig. S9 (b) shows. Therefore, it is legitimate to neglect  $q^2$ -terms under the integrals in Eq. (6). This gives

$$V_{2D}(\rho, d) \approx -\frac{1}{\rho} \int_0^\infty \frac{dx J_0(x) e^{-xd/\rho}}{1 + x(r'_0 + r''_0)/\rho}, \quad V_{2D}(\rho, 0) \approx \frac{1}{\rho} \int_0^\infty \frac{dx J_0(x)}{1 + x(r'_0 + r''_0)/\rho},$$

and the second integral turns into the KR potential energy (3) with the screening length  $r_0 = r'_0 + r''_0$ . Additionally, as per previous computational studies of monolayer TMDs [18], the monolayer screening length can be accurately represented by  $c(\varepsilon_\perp - 1)/2(\epsilon_1 + \epsilon_2)$ , where  $c$

and  $\varepsilon_{\perp}$  are the *bulk* TMD out-of-plane translation period and in-plane dielectric permittivity, respectively. For a TMD bilayer embedded in hBN with  $\varepsilon = 5.87$  (averaged over all three directions [20]), which is the case for a variety of experiments [6, 15, 16] including our experiment here, the typical parameters are  $c \approx 12 - 13$  Å,  $\varepsilon_{\perp} \approx 14 - 17$ ,  $\epsilon_1 = (2\varepsilon_{\perp} + \varepsilon_{\parallel})/3$  with  $\varepsilon_{\parallel} \approx \varepsilon_{\perp}/2$  [18, 20] and  $\epsilon_2 = \varepsilon$  (or vice versa), to yield  $r_0 \approx c(\varepsilon_{\perp} - 1)/(5\varepsilon_{\perp}/6 + \varepsilon) a_B^{*-1} < 1$  as  $a_B^*$  is consistently greater than 1 nm in TMDs both by our estimates in this work and by those of the others [16, 18]. Then, we obtain  $r_0/\rho \approx r_0/\Delta\rho_{X^{\pm}} \ll 1$ . With this in mind the denominator of the first integral above can be expanded in rapidly convergent binomial series, whereby after the term-by-term integration the interlayer electrostatic interaction energy takes the form

$$V_{2D}(\rho, d) \approx -\frac{1}{\rho} \int_0^{\infty} \frac{dx J_0(x) e^{-xd/\rho}}{1 + xr_0/\rho} \approx -\frac{1}{\sqrt{\rho^2 + d^2}} \left( 1 - \frac{d}{\rho} \frac{1}{1 + d^2/\rho^2} \frac{r_0}{\rho} + \dots \right).$$

Here, the second term in parentheses comes out as the 2nd (not the 1st as one would expect!) order of smallness since  $d/\rho \approx d/\Delta\rho_{X^{\pm}} < 1$  as demonstrated in Fig. S9 (b), and so it can be safely dropped along with the rest of higher infinitesimal order terms, whereby one arrives at the interlayer Coulomb interaction (4) we used in our calculations throughout this work. Note also that, even more generally, this series expansion can be seen to be uniformly suitable for all  $\rho \geq 0$ , including  $\rho \sim 0$  as well, in which case the second term in parentheses comes out as the 1st order of smallness in  $r_0/d$  and *still* can be dropped for  $d$  large enough, whereby one *still* arrives at Eq. (4) — now in the *classical* electrostatic Coulomb interaction regime of two space-separated point charges with intercharge distance written in cylindrical coordinates, the regime we present in the main text of this work.

## B. Particular Case of Relevance Here: IntraLayer Trion in Monolayers

The configuration space approach outlined imposes no constraints on the interlayer spacing  $d$ , which can also be seen from Fig. S9 (a) where the function  $J_{X^{\pm}}$  of Eq. (1) remains smooth and well-defined for a large range of interlayer separation distances including  $d = 0$ . Therefore, we use Eqs. (1), (2) and (5) with the  $d$  parameter set up to be equal to zero to represent a particular case of the intralayer trion we are interested in here. Plugging  $d = 0$

in there gives

$$J_{X^\pm}(\Delta\rho) = 2^{10} e^{-4\Delta\rho} \Delta\rho \left[ 1 + \frac{\Delta\rho}{4(r_0 + \left\{ \frac{1}{\sigma} \right\} \Delta\rho/\lambda)(2\Delta\rho - 1)} \right] \left( \frac{r_0 + \left\{ \frac{1}{\sigma} \right\} \Delta\rho/\lambda}{r_0 + \Delta\rho} \right)^{\frac{\lambda\Delta\rho}{\left\{ \frac{\sigma}{1} \right\} (2\Delta\rho - 1)}} \quad (7)$$

and

$$\Delta\rho_{X^\pm} = \frac{13 - \left\{ \frac{\sigma}{1/\sigma} \right\}}{8} - \left( 3 + 2 \left\{ \frac{\sigma}{1/\sigma} \right\} \right) r_0. \quad (8)$$

These are  $J_{X^\pm}$  and  $\Delta\rho_{X^\pm}$  referred to in the main text of our work. Plugging Eq. (8) in Eq. (7) with the sign reversed gives the positive  $E_{X+}$  and negative  $E_{X-}$  intralayer trion binding energies as functions of  $r_0$  and  $\sigma = m_e/m_h$ . Their absolute values are shown in Fig. S10. For  $\sigma \neq 1$  a slight difference between the two can be seen to increase with increasing  $r_0$ , the screening length parameter. Since in our experiment  $r_0$  is estimated to be small, on the order of a few hundredths within our model, we neglect this effect in our analysis presented in the main text.

### C. Remarks on the Near-Field Plasmonic Effects

There are two factors one has to care about in experiments with semiconductors located near metallic surfaces. They are associated with electronic and photonic density-of-states (DOS) modifications in the near-field zone close to the metal surface.

The image-charge approach we use in our analysis is known to break down at nanoscale distances to the surface as the screening charge cannot be localized on the metal surface due to the fundamental principles of quantum mechanics [21]. The Thomas-Fermi (TF) charge screening theory in metals takes into account the energy gain due to the screening of the external charge and the energy cost to localize the screening charge. The screening charge delocalization results in the screening at a finite wavelength  $l_{TF}$ , called the TF screening length, controlled by the *electronic* DOS at the Fermi level. The TF theory was recently extended to show a profound strength reduction for the electrostatic Coulomb interaction at distances under  $l_{TF}$ , with no change to the image-charge theory predictions otherwise [21].

Estimates of typical  $l_{TF}$  values for metals can be obtained from the ratio of their plasma frequency  $\omega_p$  to Fermi velocity  $v_F$ , that is  $l_{TF} = (\omega_p/v_F)^{-1} \lesssim 1 \text{ \AA}$ . For example, for Nb used in our experiments we have  $\omega_p = 8.87 \text{ eV}$  and  $v_F = 0.61 \times 10^8 \text{ cm/s}$  [22], to obtain  $l_{TF} \approx 0.44 \text{ \AA}$ . This is definitely a negligible quantity as compared to  $d = 15 \text{ nm}$  between the metal surface and closest TMD monolayer in our samples, suggesting that the image-charge analysis is fully legitimate in our case. Moreover, as typical van der Waals distances are known to be in the range of  $3 \div 6 \text{ \AA}$ , even a TMD monolayer placed directly on the metal surface could still be described reasonably well in terms of the electrostatic image-charge approach.

Another factor to take into consideration is local *photonic* DOS variations associated with the plasma excitations on the metal surface due to the exciton-plasmon coupling. For a dipole emitter, which is the intralayer exciton in our case, this could potentially red-shift or even split the PL emission lines, also redistributing their intensities in our experiments as one gets closer to the metal surface by decreasing the TMD monolayer-to-surface distance. Even the metal layer thickness matters in this case as per the most recent theoretical analysis [23], however, not for macroscopically thick metallic substrates with dipole-emitter-to-surface distances as large as  $d = 15 \text{ nm}$  we have in our experimental samples, so that the exciton-plasmon coupling effects can still be safely neglected.

---

[1] Y. You, X.-X. Zhang, T.C. Berkelbach, M.S. Hybertsen, D.R. Reichman, and T.F. Heinz, *Nature Physics* **11**, 477 (2015).

[2] D.W. Snoke, *Essential Concepts of Solid State Physics*, 2nd edition (Cambridge University Press, 2020).

[3] S. Y. Chen, C. X. Zheng, M. S. Fuhrer, and J. Yan, *Nano Letters* **15**, 2526 (2015).

[4] Z. Wang, Y.-H. Chiu, K. Honz, K.F. Mak, and J. Shan, *Nano. Lett.* **18**, 137 (2018).

[5] A. Arora, M. Koperski, K. Nogajewski, J. Marcus, C. Faugerasa, and M. Potemski, *Nanoscale* **7**, 10421 (2015).

[6] L.A. Jauregui, A.Y. Joe, K. Pistunova, D.S. Wild, A.A. High, Y. Zhou, G. Scuri, K. De Greve, A. Sushko, C.-H. Yu, T. Taniguchi, K. Watanabe, D.J. Needleman, M.D. Lukin, H. Park, and P. Kim, *Science* **366**, 870 (2019).

- [7] Z. Sun, J. Beaumariage, Q. Cao, K. Watanabe, T. Taniguchi, B. Hunt, and D.W. Snoke, ACS Photonics **7**, 1622 (2020).
- [8] M. Kremser, M. Brotons-Gisbert, J. Knörzer, J. Gückelhorn1, M. Meyer, M. Barbone, A.V. Stier, B.D. Gerardot, K. Müller, and J.J. Finley, npj 2D Materials and Applications **4**, 8 (2020).
- [9] I.V. Bondarev and M.R. Vladimirova, Phys. Rev. B **97**, 165419 (2018).
- [10] L.D.Landau and E.M. Lifshitz, *Quantum Mechanics. Non-Relativistic Theory* (Pergamon, Oxford, 1991).
- [11] I.V. Bondarev, Mod. Phys. Lett. B **30**, 1630006 (2016).
- [12] I.V. Bondarev, O.L. Berman, R.Ya. Kezerashvili, and Y.E. Lozovik, arXiv:2002.09988.
- [13] R.P. Leavitt and J.W. Little, Phys. Rev. B **42**, 11774 (1990).
- [14] L.V. Keldysh, Sov. Phys. JETP **29**, 658 (1979); N.S. Rytova, Proc. MSU Phys. Astron. **3**, 30 (1967).
- [15] G. Wang, A. Chernikov, M.M. Glazov, T.F. Heinz, X. Marie, T.Amand, and B.Urbaszek, Rev. Mod. Phys. **90**, 021001 (2018).
- [16] M.Goryca, J.Li, A.V.Stier, T.Taniguchi, K.Watanabe, E.Courtade, S.Shree, C.Robert, B.Urbaszek, X.Marie, and S.A.Crooker, Nature Commun. **10**, 4172 (2019).
- [17] P.Cudazzo, I.V.Tokatly, and A.Rubio, Phys. Rev. B **84**, 085406 (2011).
- [18] T.C. Berkelbach, M.S. Hybertsen, and D.R. Reichman, Phys. Rev. B **88**, 045318 (2013).
- [19] N.A. Asriyan, I.L. Kurbakov, A.K. Fedorov, and Yu.E. Lozovik, Phys. Rev. B **99**, 085108 (2019).
- [20] A. Laturia, M.L. Van de Put, and W.G. Vandenberghe, npj 2D Mater Appl **2**, 6 (2018).
- [21] V. Kaiser, J. Comtet, A.Nigès, A. Siria, B. Coasne, and L. Bocquet, Faraday Discuss. **199**, 129 (2017).
- [22] B. Chakraborty, W.E. Pickett, and P.B. Allen, Phys. Rev. B **14**, 3227 (1976).
- [23] I.V. Bondarev, H. Mousavi, and V.M. Shalaev, Phys. Rev. Research **2**, 013070 (2020).
- [24] M. Barbone et al., “Charge-tunable biexciton complexes in monolayer WSe<sub>2</sub>,” Nature Comm. **9**, 3721 (2018).
- [25] S.-Y. Chen, T. Goldstein, T. Taniguchi, K. Watanabe and J. Yan, “Coulomb-bound four- and five-particle intervalley states in an atomically-thin semiconductor,” Nature Comm. **9**, 3717

(2018).

[26] Z. Li, et al., “Revealing the biexciton and trion-exciton complexes in BN encapsulated WSe<sub>2</sub>,” *Nature Comm.* **9**, 3719 (2018).

[27] Z. Ye et al., “Efficient generation of neutral and charged biexcitons in encapsulated WSe<sub>2</sub> monolayers,” *Nature Comm.* **9**, 3718 (2018).

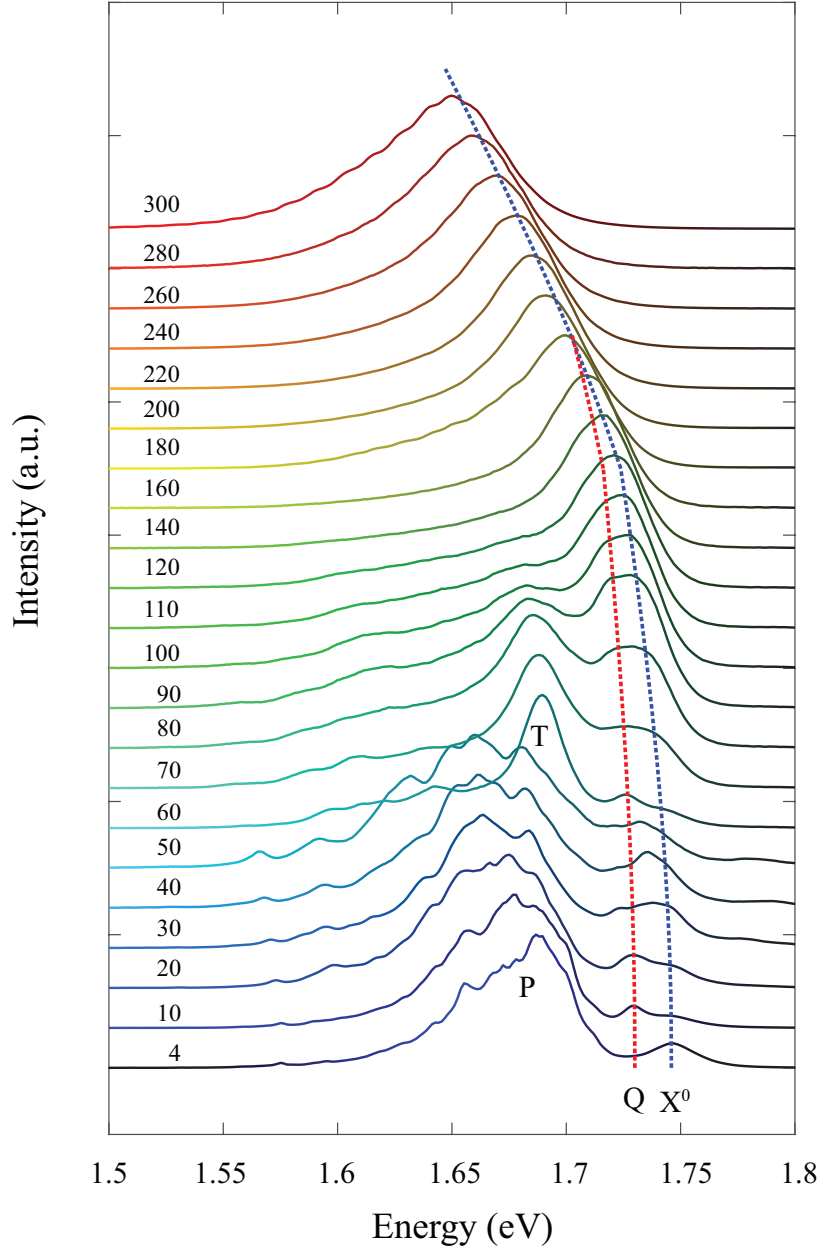


FIG. S1. Second sample with the same structure as the sample discussed in the main text. The direct exciton is seen at about the same energy, equal to 1.747 eV at low temperature, and the quaternion line is also clearly identifiable at low temperature. The trion line (seen most clearly at around  $T = 100$  K) also appears at the same energy, about 40 meV below the exciton line. The dashed lines are fits to the shift of the lines predicted by the Varshni formula for band gap shift.

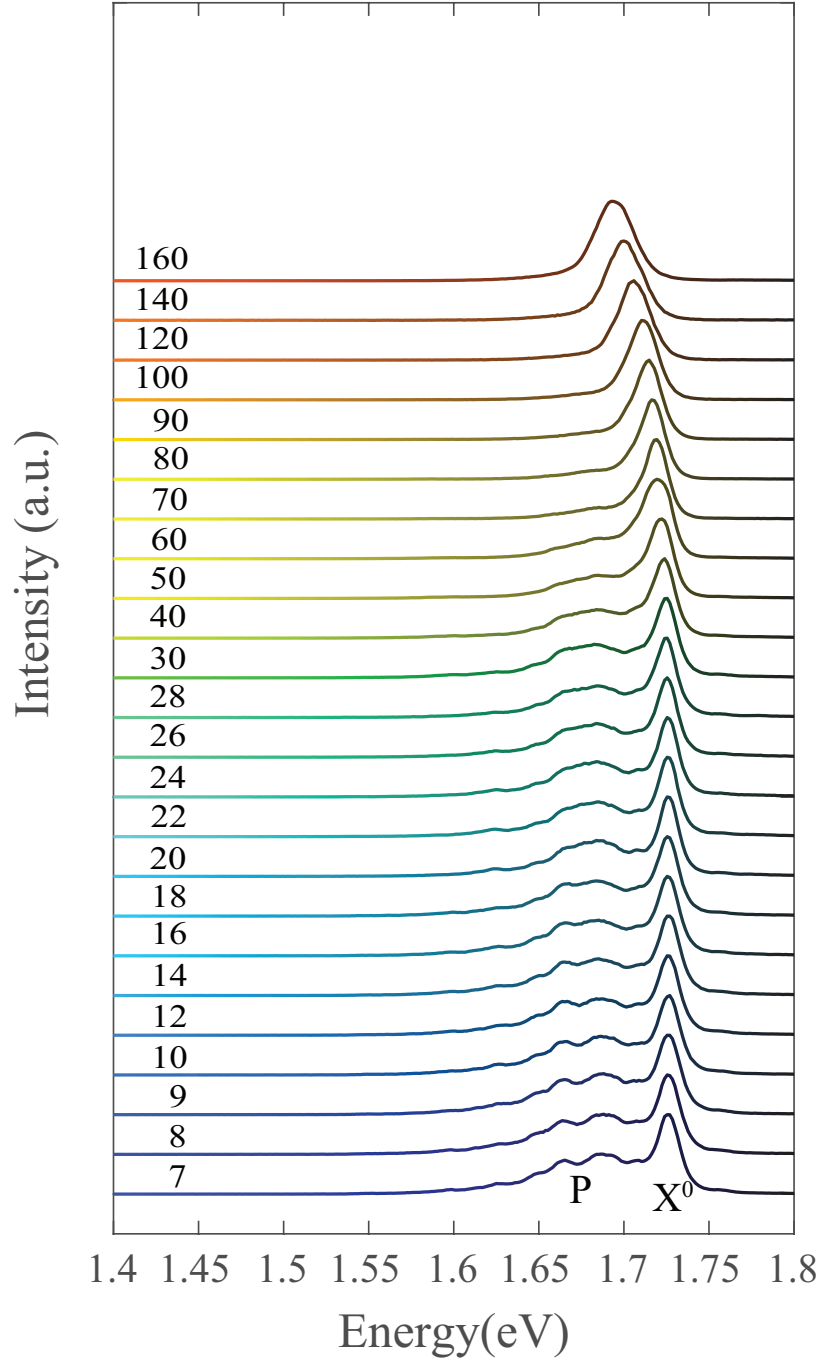


FIG. S2. Control sample #1, consisting of one undoped monolayer of WSe<sub>2</sub> encapsulated in hBN, with no metal layer. The direct exciton line dominates the whole spectrum. Its energy is about 15 meV lower than for all samples with a metal layer, indicating slightly stronger exciton binding when there is no image charge of the metal. No quaternion line is seen, and trion emission is either absent or buried in the impurity emission.

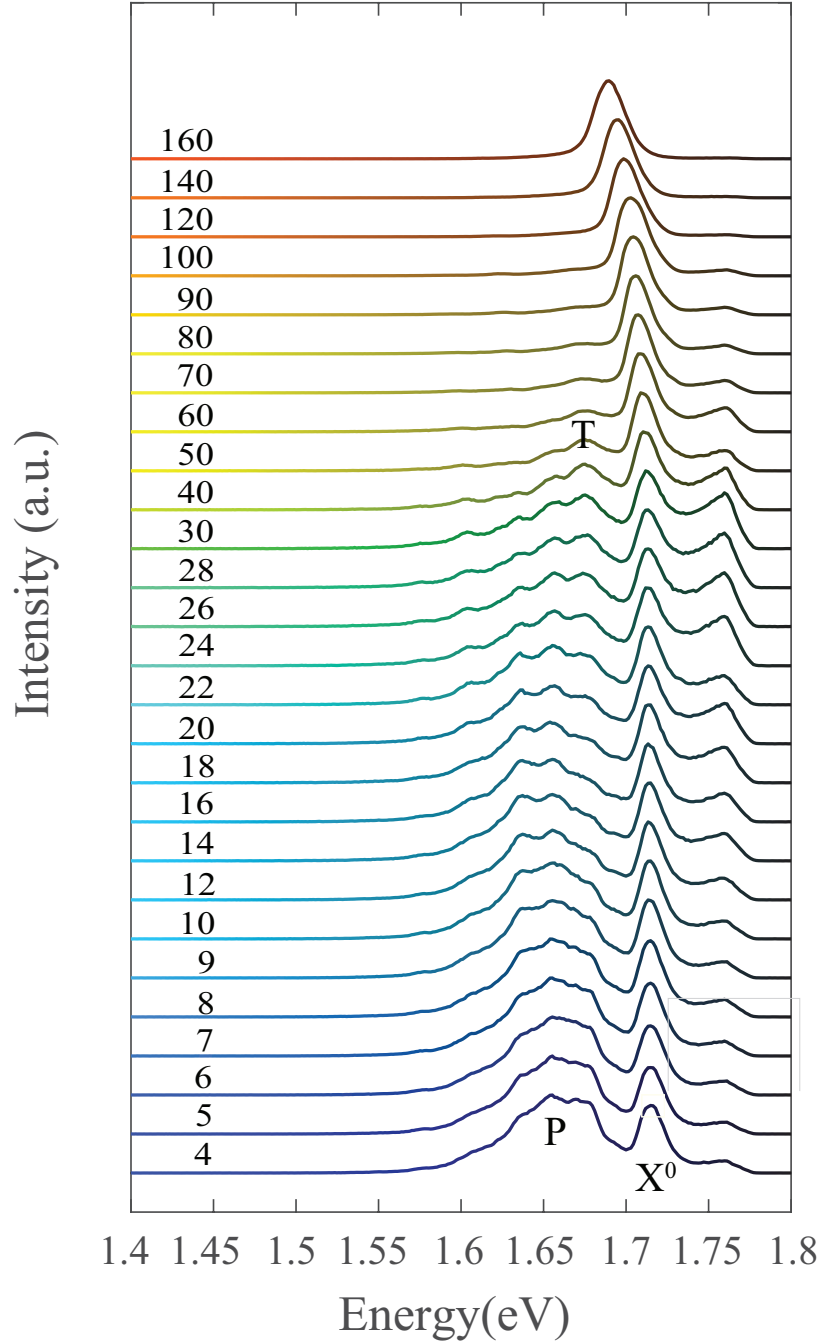


FIG. S3. Control sample #2, consisting of one p-doped monolayer of WSe<sub>2</sub> encapsulated in hBN, with no metal layer. The direct exciton line appears at the same energy as control sample #1, which also had no metal layer. The peak above 1.75 eV is an artifact of scattered light cut off by a 700-nm long-pass filter.

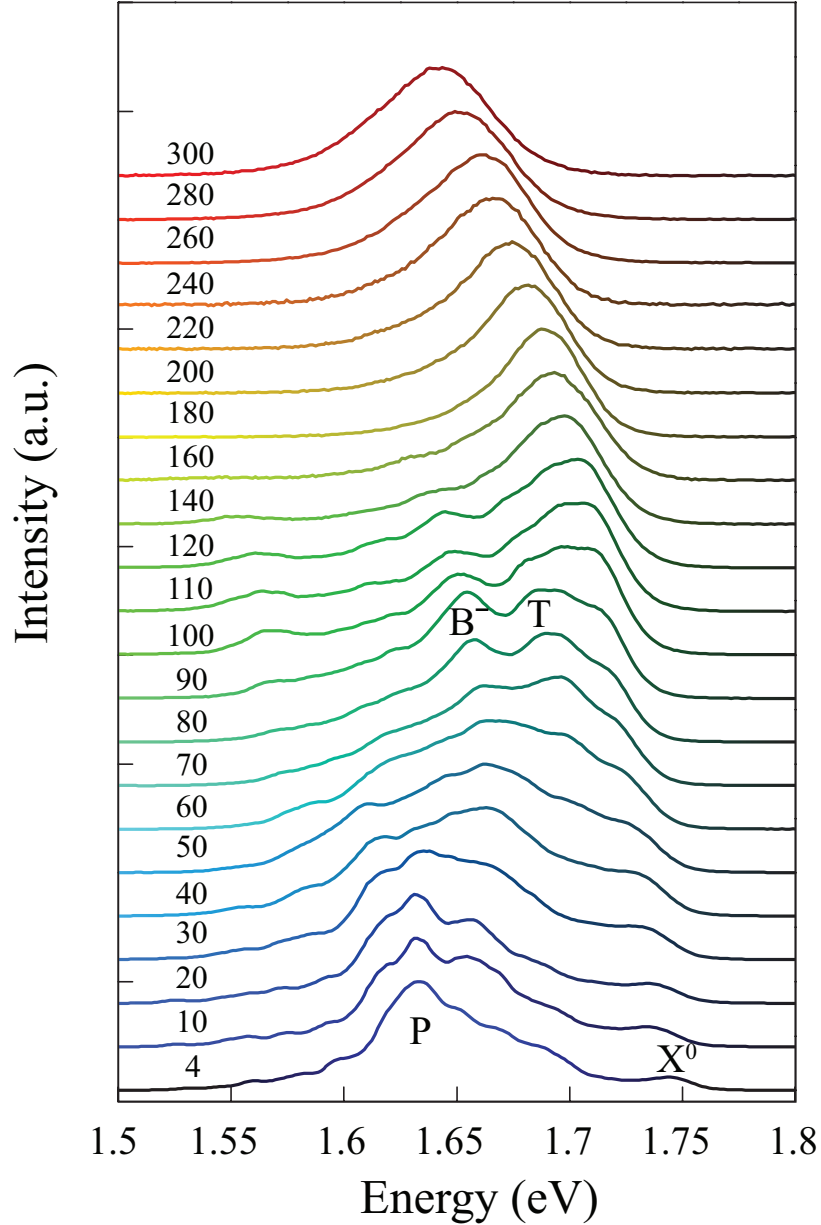


FIG. S4. Control sample #3, consisting of one p-doped monolayer of WSe<sub>2</sub> in the presence of a metal layer. The thickness of the hBN layer between the monolayer and the metal was 15 nm. The direct exciton and trion lines appear at the same energies as for the bilayer stacks in the presence of a metal layer; a charged biexciton line (B<sup>-</sup>) is visible at 1.65 eV at  $T = 100$  K. No quaternion line is seen.

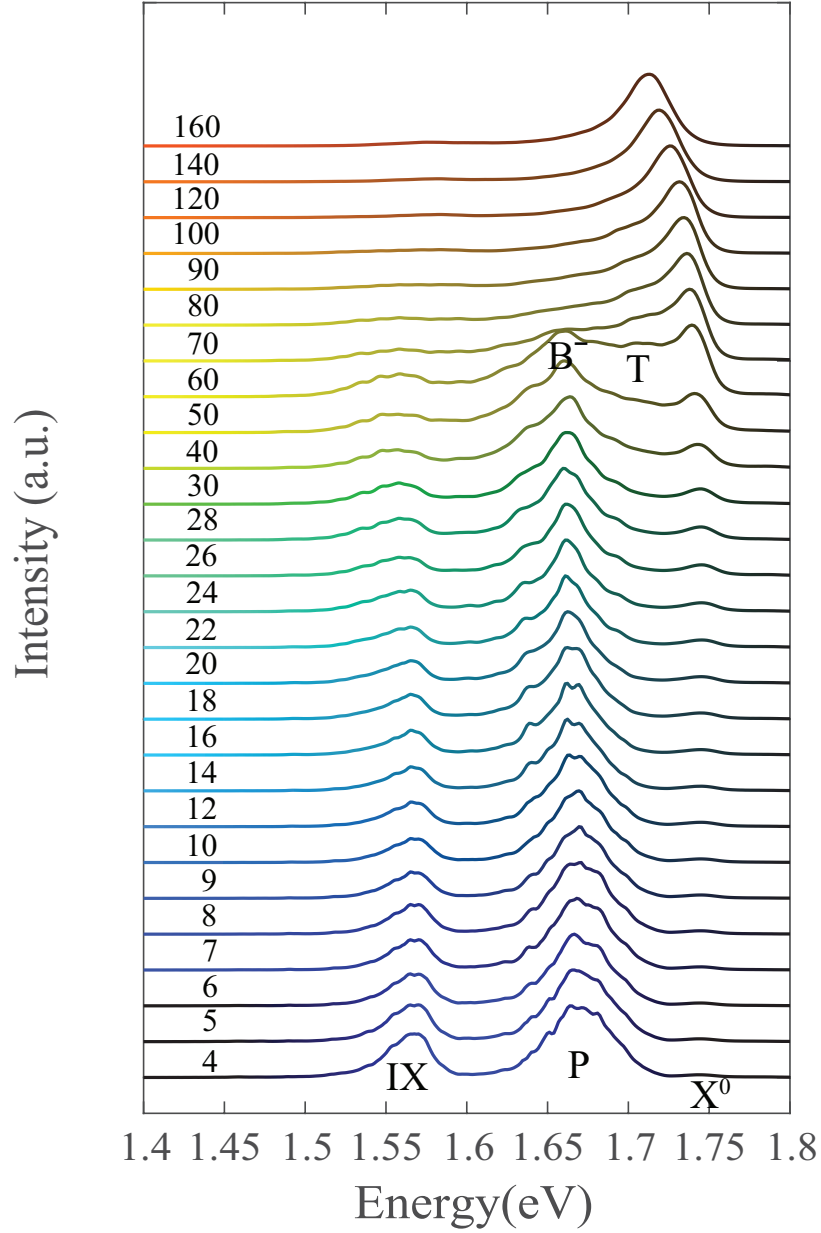


FIG. S5. A second WSe<sub>2</sub>-based sample with the same structure as the sample discussed in the main text, but without the metal layer, and with the hBN layer between the monolayers much thinner, approximately 2 nm. The direct exciton is seen at the same energy position, close to 1.75 eV at low temperature, but the quaternion line is not seen. An interlayer exciton (IX) is seen prominently at 1.57 eV at low temperature, while the trion line is suppressed or buried in the impurity PL, and the quaternion line not seen. This sample, and other measurements of its PL properties, such as time-resolved PL showing a long lifetime for the IX, is discussed in another publication [7].

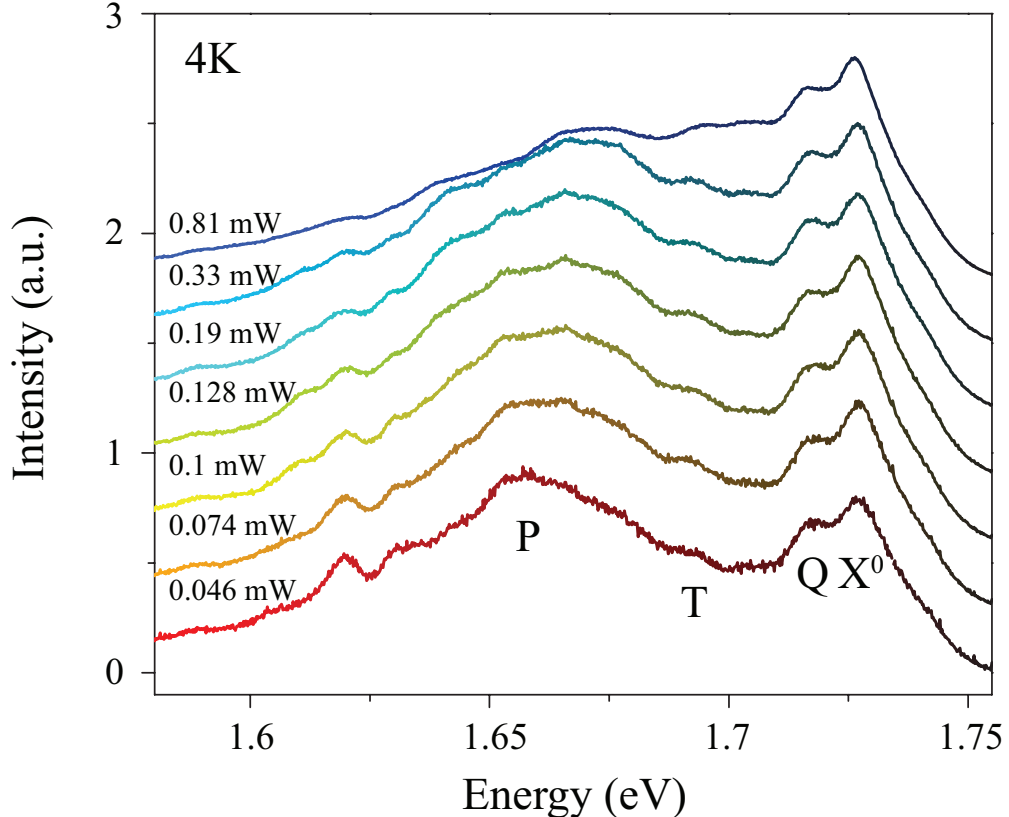


FIG. S6. A power sequences experiment was carried out upon a third WSe<sub>2</sub>-based sample with the same structure as the sample discussed in the main text pumped with a 532 nm Nd: YAG laser at 4K. An equal energy redshift of the exciton and quaternion lines is observed due to the laser heating effect. The direct exciton is seen at 1.726 eV, and the quaternion line is also clearly identifiable around 1.714 eV. The trion line here is 1.69 eV, about 36 meV below the exciton line. A saturation of the intensity of the impurity is unambiguously seen, which is different from the behavior of the exciton and the quaternion.

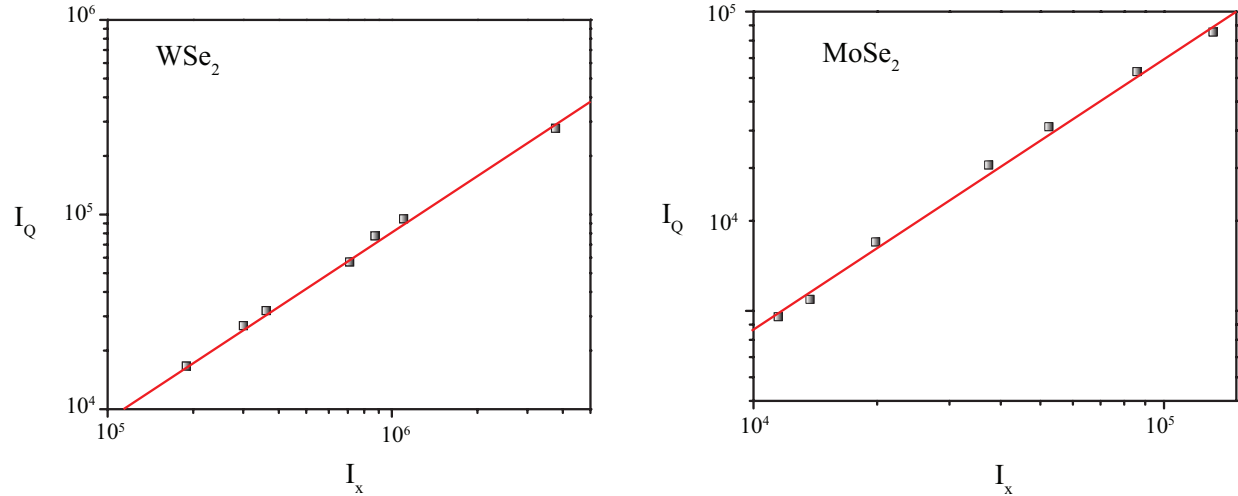


FIG. S7. Intensity of the quaternion PL as a function of the exciton intensity PL for both  $\text{WSe}_2$  and  $\text{MoSe}_2$  stacks. Q line has a clear linear dependence as the red line shows, not superlinear. And the Q line appears only in doped bilayers with metal.

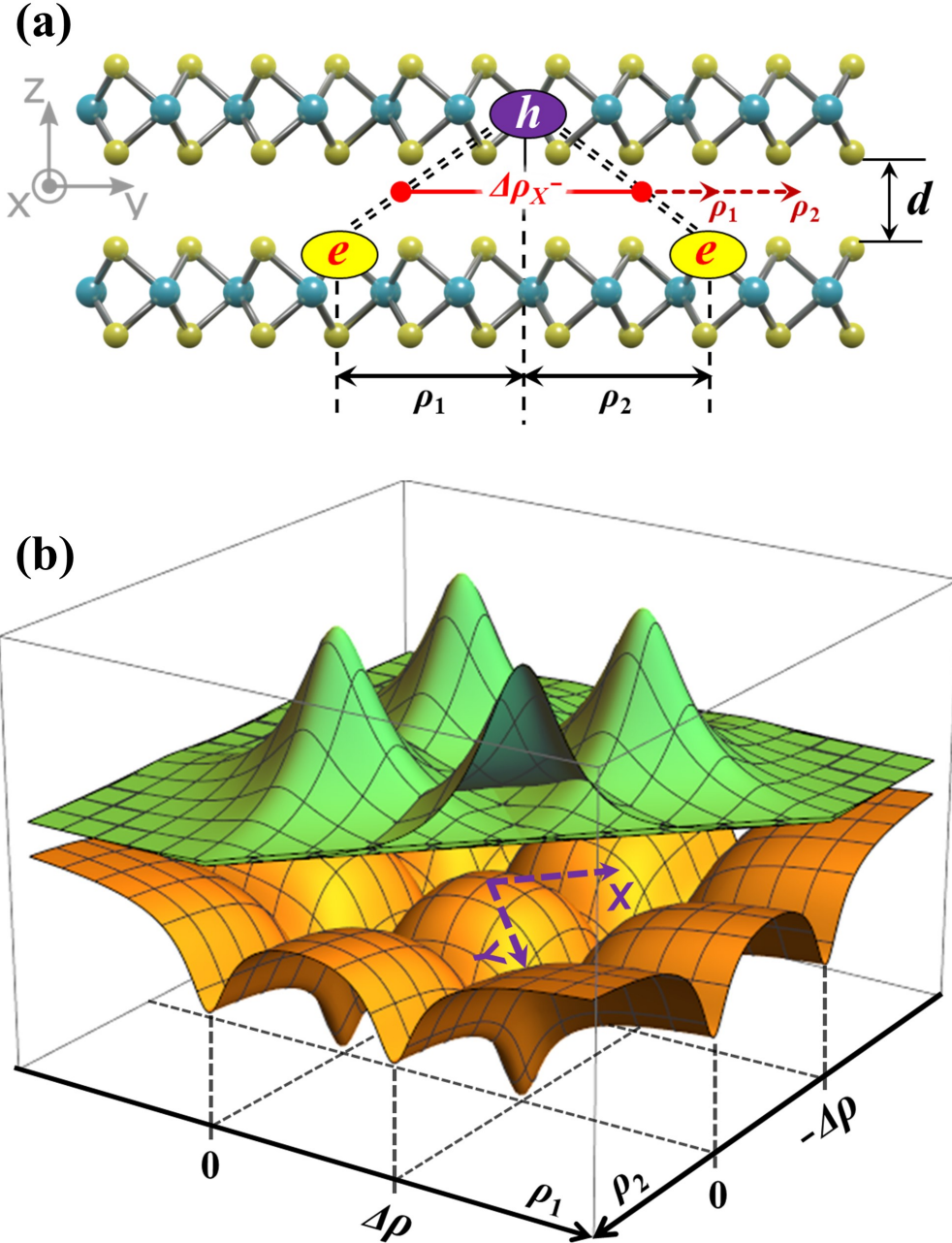


FIG. S8. (a) The structure of a negatively charged interlayer exciton (CIE) in a TMD bilayer. (b) Schematic of the tunnel exchange coupling configuration for the two ground-state indirect excitons (IEs) to form the CIE complex in (a). The coupling occurs in the configuration space of the two *independent* in-plane relative  $e$ - $h$  motion coordinates,  $\rho_1$  and  $\rho_2$ , of each of the IEs separated by the center-of-mass-to-center-of-mass distance  $\Delta\rho$  — cf. (a). The coupling is due to the tunneling of the  $e$ - $h$  system in  $x$  (or  $y$ ) direction through the potential barrier formed by the two  $e$ - $h$  electrostatic interaction potentials of the two IEs (bottom, orange color), between the equivalent IE states represented by the two-exciton wave function shown on the top (green color).

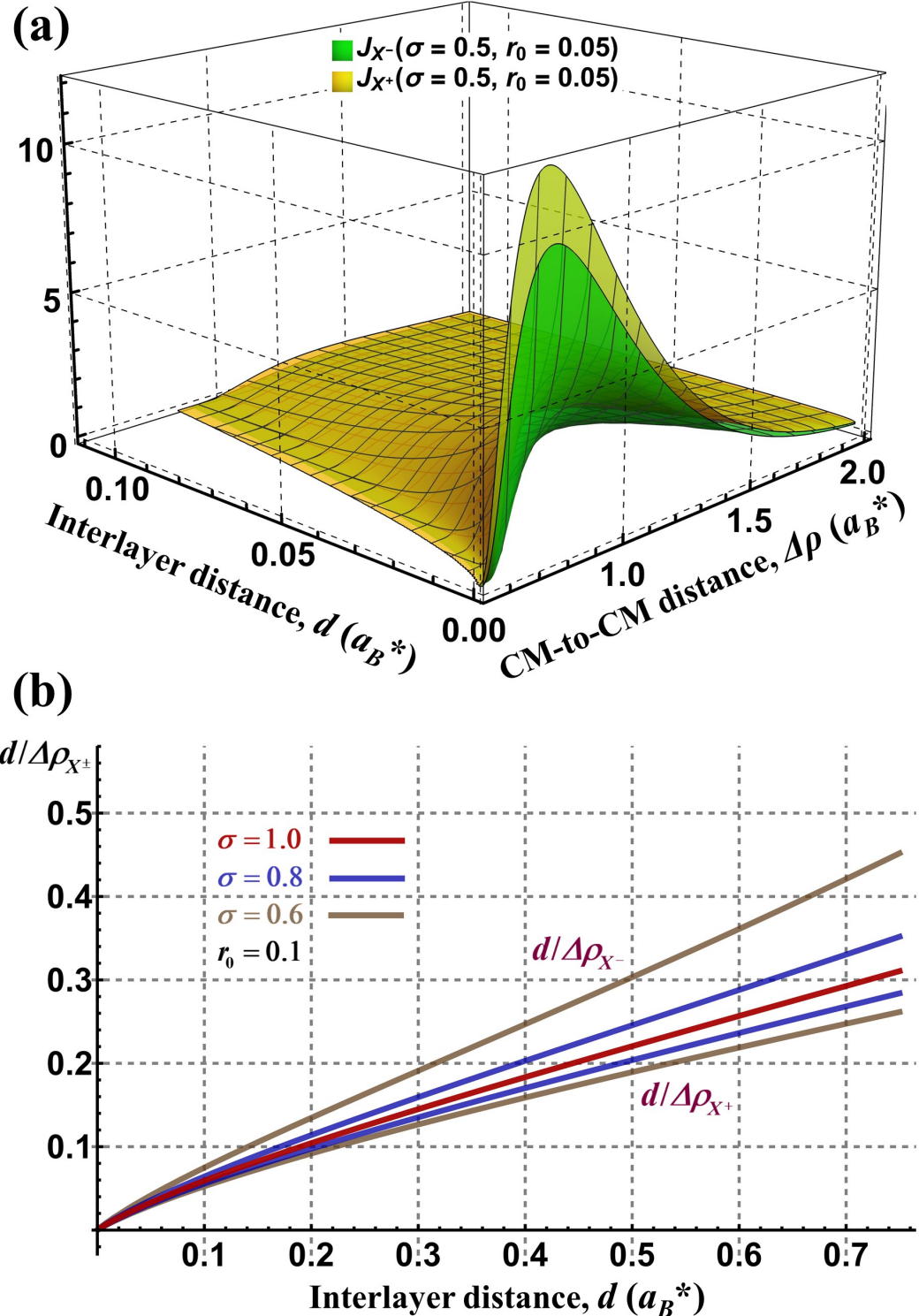


FIG. S9. (a) The exchange tunneling rate integral  $J_{X^\pm}$  as a function of  $d$  and  $\Delta\rho$ , calculated per Eqs. (1) and (2) for a bilayer with  $d$  in the range not to exceed typical van der Waals interlayer separations. (b) The equilibrium  $d/\Delta\rho_{X^\pm}$  ratio as given for a similar  $d$  range by Eq. (5) with typical values of other intrinsic parameters of the bilayer system.

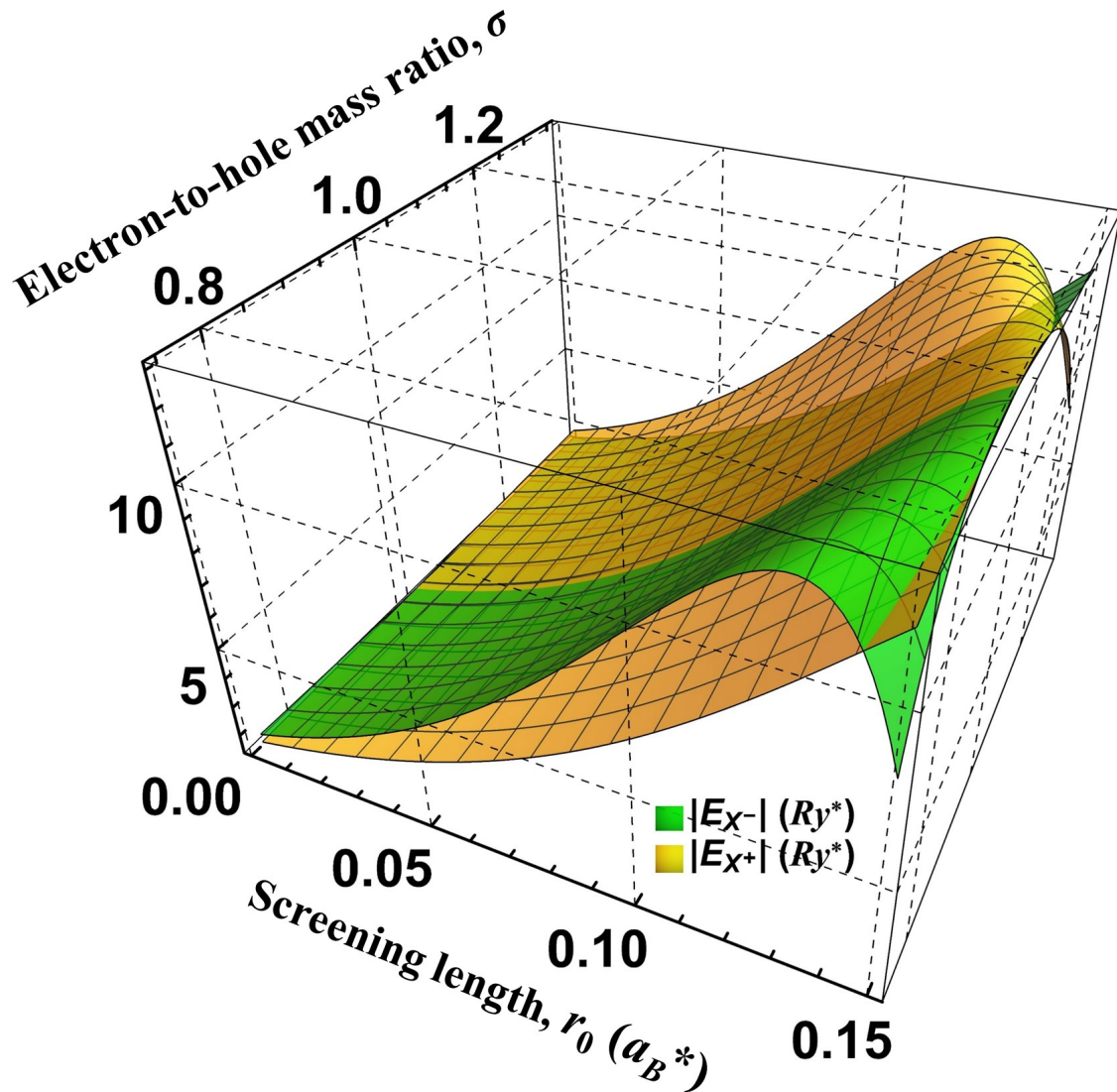


FIG. S10. The absolute values of the positive and negative intralayer trion binding energies for a range of  $r_0$  and  $\sigma$  parameters as given by Eqs. (7) and (8).